Spectral Imaging System Analytical Model for Subpixel Object Detection

John P. Kerekes, *Senior Member, IEEE,* and Jerrold E. Baum

Abstract—Data from multispectral and hyperspectral imaging systems have been used in many applications including land cover classification, surface characterization, material identification, and spatially unresolved object detection. While these optical spectral imaging systems have provided useful data, their design and utility could be further enhanced by better understanding the sensitivities and relative roles of various system attributes; in particular, when application data product accuracy is used as a metric. To study system parameters in the context of land cover classification, an end-to-end remote sensing system modeling approach was previously developed. In this paper, we extend this model to subpixel object detection applications by including a linear mixing model for an unresolved object in a background and using object detection algorithms and probability of detection (P_D) versus false alarm (P_{FA}) curves to characterize performance. Validations with results obtained from airborne hyperspectral data show good agreement between model predictions and the measured data. Examples are presented which show the utility of the modeling approach in understanding the relative importance of various system parameters and the sensitivity of P_D versus P_{FA} curves to changes in the system for a subpixel road detection scenario.

Index Terms—Hyperspectral imaging, multispectral imaging, remote sensing system modeling, subpixel object detection.

I. INTRODUCTION

SPECTRAL imaging sensors and their applications have evolved tremendously over the past three decades. Table I presents examples of the progression in technology for both airborne and spaceborne sensors [1]. Enabled by this technology, the sophistication of the application products has increased as well. The evolution from multispectral to hyperspectral sensors such as AVIRIS [2], HYDICE [3], and Hyperion [4], has improved land cover class differentiation [5], remote material identification [6], and subpixel object detection [7].

As the technology has evolved to support finer spectral and spatial resolution, the amount of data collected (and information that can be extracted) has increased tremendously, as shown in the right hand column of Table I. This increase in data complexity has motivated research in new methods to optimally process the data and efficiently extract the desired information [8]. These methods rely more on computer processing and less on visual interpretation by an analyst.

The tremendous data volume associated with these sensors also motivates targeted, efficient instrument design and collection methods to acquire the necessary data without drowning in that which is irrelevant. While a strength of modern hyperspectral sensors is that they collect comprehensive data that can be used in a variety of applications, for any given application much of the data may go unused. Also, data collected under some illumination or environmental conditions may not even contain the desired information. There is a cost to collecting these data in terms of instrument complexity, data storage, communications, processing requirements, and missed opportunities to collect data elsewhere. It is, therefore, becoming increasingly important to design and operate these sensors in ways that optimize the probability of collecting sufficient (quantity and quality), but not excessive, data to extract the desired information about a remote scene. Also, because the complexity of these data require automated algorithms, as opposed to analyst visual interpretation, the traditional design metrics of instrument performance (spatial resolution, radiometric accuracy, optical quality, etc.) are only part of what ultimately determines the amount of information that can be extracted from the data. In this sense, it is recognized that there needs to be a better understanding of the interactions among instrument capability, the characteristics of the scene, and the data extraction algorithms.

It is this goal of moving toward a more optimal (judged by an application product metric) design and use of spectral imaging sensors that motivates our development of spectral imaging remote sensing system models. By building models of the remote sensing process and understanding the key contributors to system performance, we can better design, operate, and task these systems. These models also help us to better understand the potential performance and the limitations of spectral imaging technology. This, of course, is a very challenging goal, and the specifics will depend on particular systems and applications, but the complexity of the systems and the potential payoffs offer strong motivation for this work.

To this end, we have been developing end-to-end spectral imaging system models that include significant effects of the remote sensing process, including those from the information extraction algorithms. Previous work developed such a model in the context of land cover classification [9], [10]. This modeling approach uses statistical representations of various land cover classes and analytically propagates them through the remote sensing system. A similar approach was adopted by Schwartz *et al.* [11], to analyze multispectral sensor systems in mine detection applications. These statistical approaches contrast with image simulation models such as HySIM [12], [13] and DIRSIG [14], which produce synthetic images suitable for analysis with

TABLE I
EXAMPLE SPECTRAL IMAGING SENSORS (a) AIRBORNE AND (b) SPACEBORNE

A) AIRBORNE

Initial Year	Sensor Name	Nominal Altitude	Spectral Channels	Spatial Resolution	Radiometric Bits	Raw Data Volume (Kbytes/sq. km)
1971	M-7	4 km	12	10 m	8	120
1986	AVIRIS	20 km	224	20 m	12	840
1994	HYDICE	6 km	210	3 m	12	35,000

B) SPACEBORNE

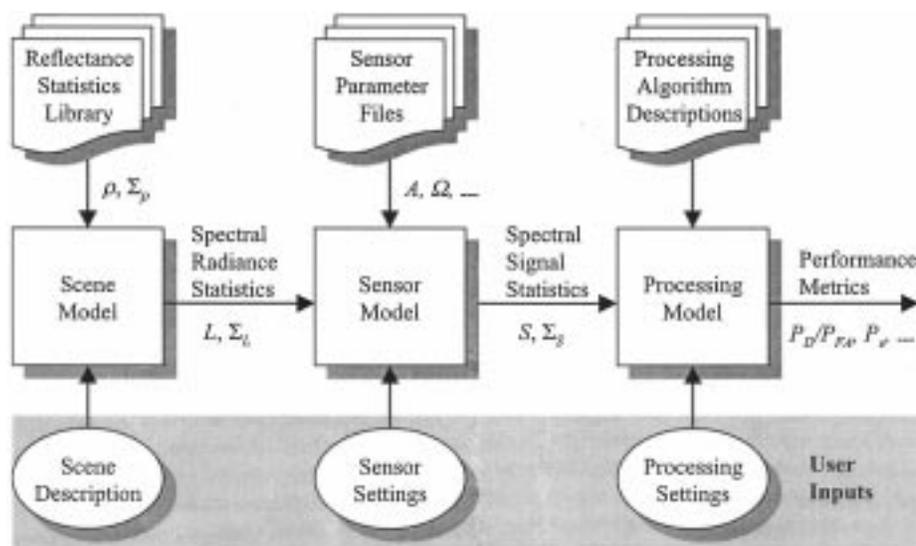| Initial Year	Sensor Name	Satellite Platform	Spectral Channels	Spatial Resolution	Radiometric Bits	Raw Data Volume (Kbytes/sq. km)
1972	MSS	ERTS-1	4	80 m	8	0.6
1982	TM	Landsat-4	7	30 m	8	7.8
2000	Hyperion	EO-1	220	30 m	12	366.7

Fig. 1. Block diagram of spectral imaging system analytical model. The diagram shows the flow of the spectral mean and covariance statistics from the reflectance library through the scene and sensor models, and then being operated on in the processing model to predict a performance metric. Symbols are defined in the text.

traditional tools. The statistical analytical models do not produce an image, but rather represent the characteristics of the scene classes by statistical models, and compute expected performance through the use of analytical equations. This approach offers the advantages of reduced manual scene definition and computational time, allowing tradeoff and sensitivity analyses to be conducted quickly, but with the disadvantage of not being tractable for certain situations involving nonlinear effects.

This analytical modeling approach has now been extended to model the detection of subpixel surface objects through the use of a linear mixing model for an object in a given background and the inclusion of object detection algorithms and metrics. This paper documents these model enhancements through a description of the model theory (Section II), validations of the model (Section III), and examples of typical results obtained from analyses conducted with the model (Section IV). The paper concludes with a summary and discussion of the model's limitations, including areas of ongoing research to overcome these limitations (Section V).

II. ANALYTICAL MODEL DESCRIPTION

The underlying premise of the model is that the various surface classes of interest can be represented by first- and second-order spectral statistics and that the effects of various processes in the end-to-end spectral imaging system can be modeled as transformations and functions of those statistics. The end-to-end system includes the scene (illumination, surface, and atmospheric effects), the sensor (spatial, spectral, and radiometric effects), and the processing algorithms (calibration, feature selection, application algorithm) that produce a data product. The model described here is based upon our previous work [9].

Fig. 1 presents a block diagram of the model and associated supporting data files. The model is driven by a user-specified input set of system parameter settings that define the scenario, including the scene classes, atmospheric state, sensor characteristics, and processing algorithms. Table II contains a list of scenario parameters and options available, as well as their symbols used in this paper.

TABLE II
INPUT SYSTEM PARAMETERS AVAILABLE IN MODEL

Scenario Parameter	Symbol and Possible Values
Scene	
Surface classes	M (≥ 2), from spectral statistics library
Area fraction occupied by class m	$0 < f_m < 1$, $\Sigma f_m = 1$
Pixel fraction occupied by sub-pixel object	$0 < f_T < 1$
Object fraction in shadow	$0 < f_S < 1$
Fraction of sky visible for object in shadow	$0 < f_{sky} < 1$
Spectral covariance scaling factor for class m	g_m
Solar zenith angle	$0 \leq \theta_s < 90°$
Atmospheric model	tropical, mid-latitude summer, mid-latitude winter, sub-arctic summer, sub-arctic winter, 1976 US standard
Meteorological range (visibility)	V
Aerosol model	rural or urban
Cloud at 2.4 km altitude	Yes or no
Sensor	
Sensor Type	
Number of spectral channels	N
Channel wavelengths	λ
Channel bandwidths	$\Delta\lambda$
Spectral quantum efficiency	η
Spectral optics transmittance	τ
Pixel integration time	t
Saturation spectral radiance	L_{max}
Number of radiometric bits	Q
Sensor platform altitude	z
Sensor nadir view angle	$0 \leq \theta_s < 90°$, nadir $= 0°$
Sensor noise factor	g_n
Relative calibration error	c_R
Data bit error rate	B_e
Processing	
Number of features	F
Spectral regions for use as features	Wavelength regions
Feature selection algorithm	Contiguous regions, principle components, band averaging
Atmospheric compensation	ELM or none
Performance algorithm metric	CEM spectral matched filter, total error, spectral characterization accuracy
Desired false alarm rate	$10^{-6} < P_{FA} < 10^{-2}$

These parameters are used in analytical functions to transform the spectral reflectance first- and second-order statistics of each surface class through the spectral imaging process. The spectral mean and spectral covariance matrix of each class is propagated from reflectance to spectral radiance to sensor signals and, then, to features, where they are operated on to achieve a metric of system performance. The following sections describe the scene, sensor, and processing components of the model, as well as a brief description of the model implementation.

A. Scene Model

The model considers a scene to consist of one, or more, background classes and an object class. The user supplies the proportion of the scene filled by each background class and the fraction of a pixel occupied by the object class. Each class is described by its first- and second-order spectral reflectance statistics (mean and covariance). Weighted combinations of these reflectance vectors and matrices, along with descriptions of the atmosphere and the observation geometry, are transformed by an atmospheric code into surface-reflected and path-scattered radiances. These radiances are then combined to produce the mean and covariance statistics of the spectral radiance at the input aperture of a spectral imaging sensor. The notional scene geometry, reflectance inputs, transformations, and at-sensor radiance are detailed below.

1) Notional Scene Geometry and Subpixel Object Model: The model assumes a simple area-weighted linear mixing model for a subpixel object within a scene that contains one or more background classes. Each of the M background classes occupies a fraction f_m of the scene, with the constraint the fractions sum to one. The subpixel object is considered to be embedded within one of these classes, denoted m^*. It is important to note that this model does not actually simulate a specific spatial layout, but rather accounts for the effects of the multiple background classes through the area-weighting scheme.

A simple linear model is assumed for the object-class pixel. The subpixel fraction f_T ($0 < f_T \leq 1$) defines the fractional area of the pixel occupied by the object with direct line-of-sight to the sensor. Parts of the object occluded by the background are accounted for in the background fraction. The fraction of the object in shadow, f_S, ($0 \leq f_S \leq 1$) is illuminated only by diffuse sky irradiance, assuming the structure casting the shadow is opaque. In cases where $f_S > 0$, the fractional amount of the sky's full hemisphere visible from the object, f_{sky}, ($0 < f_{sky} \leq 1$) must be specified. This allows for a situation where the full hemisphere of downwelling sky irradiance may be partially blocked, (e.g., an object on the ground between tall trees), and only a fraction of the sky is visible from the object. In these cases, the amount of diffuse, or sky, radiance is reduced proportionally by f_{sky}.

2) Input Reflectance Statistics: The object and background spectral reflectance statistics are computed externally and provided as inputs to the model. They may be derived from airborne spectrometer imagery converted to reflectance, field spectrometers, laboratory measurements, or physics-based simulations. For each class, the input statistics consist of a K-dimensional spectral mean reflectance vector ρ and a $K \times K$ reflectance spectral covariance matrix Σ_ρ.

The model assumes that the reflectance distribution of each class, background or object, is unimodal. Thus, the data used to compute the statistics must be carefully screened, through spectral clustering or histogram techniques, to ensure they form a cluster around a single mean point in the K-dimensional space. In some cases, a single terrain category will need to be separated into multiple reflectance classes to ensure each class is unimodal. For example, the single category "grass" may need to be split into "dry grass" and "healthy grass" classes, each with a different mean reflectance. Also, the model considers the reflectance vectors to be hemispherical reflectance factors for completely diffuse surfaces. BRDF effects are not considered.

3) Atmospheric Radiance and Transmittance: The model uses the Air Force Research Laboratory code MODTRAN [15] to compute the solar illumination and atmospheric effects. A number of calls are made to the code to calculate the various radiance vectors used to transform the reflectance statistics to radiance statistics. For convenience in the current version of the software, the sensor channel spectral response functions are convolved with the spectral radiances immediately after each MODTRAN run is completed. Thus, the spectral radiance vectors at the output of the scene model have the same dimensionality as the sensor.

4) Mean Spectral Radiance[1]:

The total mean spectral radiance for each class is the sum of $L_S(\rho)$, the total surface reflected radiance for a mean surface reflectance ρ and $L_P(\rho_{ave})$, the scattered path radiance calculated with the scene average reflectance ρ_{ave} as the surface albedo. This formulation for the path radiance models the "adjacency effect" and is discussed below. The model has been developed for sensors operating in the reflective solar portion of the optical spectrum, with scenes near room temperature; thus, thermal emission effects are not considered.

[1]Note: All radiance calculations are performed as functions of wavelength, but, for clarity in presentation, the subscript λ has been dropped.

Background(s): A separate call to MODTRAN is made for each of the M background classes, as well as one for the scene average case. The total mean spectral radiance for each case is as shown in (1) and (2)

$$L_{Bm} = L_S(\rho_m) + L_P(\rho_{ave}) \tag{1}$$

$$L_{Bave} = L_S(\rho_{ave}) + L_P(\rho_{ave}). \tag{2}$$

The scene average reflectance, ρ_{ave}, is computed using the class fractions f_m as in (3)

$$\rho_{ave} = \sum_{m=1}^{M} f_m \rho_m. \tag{3}$$

Object Fully Illuminated: When the object is in the open (no shadows present) the mean spectral radiance for the object class is as shown in (4)

$$\tilde{L}_T = L_S(\tilde{\rho}_T) + L_P(\rho_{ave}). \tag{4}$$

The surface albedo used in the MODTRAN call to generate the first term of equation (4) is computed as in (5). The weighted sum of the object class mean reflectance and the background class m^* mean reflectance implements the linear model described above

$$\tilde{\rho}_T = f_T \rho_T + (1 - f_T)\rho_{m^*}. \tag{5}$$

Object in Shadow: When the object is in full or partial shadow, the calculation is done slightly differently to handle the various sources of illumination. Equation (6) shows the mean object spectral radiance for this case

$$\tilde{L}_T = f_T[(1 - f_S)L_{SD}(\rho_T) + f_{sky}(L_S(\rho_T) - L_{SD}(\rho_T))] \\ + (1 - f_T)L_S(\rho_{m^*}) + L_P(\rho_{ave}). \tag{6}$$

L_{SD} is the direct (from the sun) ground reflected radiance, whereas L_S is the total (including sky irradiance) ground reflected radiance. Thus, the contribution from the sky irradiance is assumed to be the difference $L_S - L_{SD}$.

Path Radiance Calculation: For all mean spectral radiance calculations, the path-scattered contribution L_P is calculated using the scene fractional area-weighted average reflectance ρ_{ave} as shown in (3). (Note that when MODTRAN is run with the multiple scattering option on, the atmospheric scattered path radiance term depends on the surface albedo.) This approach accounts for the "adjacency effect," which is the scattering of nearby surface reflected radiance into the sensor's instantaneous field-of-view (IFOV). The assumption here is that the scattering scale of the effect covers the entire scene being collected. Studies have shown this effect can occur out to several hundred meters [16], typical of the scenes considered by the model.

5) Spectral Radiance Covariance: The transformation of the spectral reflectance covariance statistics to spectral radiance covariance statistics follows the same linear atmospheric model assumed in the mean calculations. The idea behind the transformation is to interpolate spectral radiances calculated for surface albedos equal to zero and one by using the entries of the reflectance covariance matrices. These transformations

use the following diagonal matrices, with the described vectors along the diagonals and zeros elsewhere

Λ_{LS1} total surface reflected spectral radiance for a surface albedo of 1;

Λ_{LD1} direct surface reflected spectral radiance for a surface albedo of 1;

Λ_{LP1} atmospheric path scattered spectral radiance for a surface albedo of 1;

Λ_{LP0} atmospheric path scattered spectral radiance for a surface albedo of 0.

Background Classes: The background spectral radiance covariance matrices for each of the M background classes and the scene average are computed as shown in (7) and (8). g_{CB} is a user-specified scalar used to study the effect of scaling the background covariance matrices

$$\Sigma_{LBm} = \Lambda_{LS1}g_{CB}\Sigma_{\rho Bm}\Lambda_{LS1} + [\Lambda_{LP1} - \Lambda_{LP0}]g_{CB}$$
$$\cdot \Sigma_{\rho Bave}[\Lambda_{LP1} - \Lambda_{LP0}] \tag{7}$$
$$\Sigma_{LBave} = \Lambda_{LS1}g_{CB}\Sigma_{\rho Bave}\Lambda_{LS1} + [\Lambda_{LP1} - \Lambda_{LP0}]g_{CB}$$
$$\cdot \Sigma_{\rho Bave}[\Lambda_{LP1} - \Lambda_{LP0}]. \tag{8}$$

Object Fully Illuminated: The object class spectral radiance covariance matrix is computed using the total surface reflected radiance output from MODTRAN as shown in (9). g_{CT} is similar to g_{CB}, defined above, but for the object class

$$\Sigma_{LT} = f_T^2\Lambda_{LS1}g_{CT}\Sigma_{\rho T}\Lambda_{LS1} + (1 - f_T)^2\Lambda_{LS1}g_{CB}\Sigma_{\rho Bm^*}$$
$$\cdot\Lambda_{LS1} + [\Lambda_{LP1} - \Lambda_{LP0}]g_{CB}\Sigma_{\rho Bave}[\Lambda_{LP1} - \Lambda_{LP0}]. \tag{9}$$

Object in Shadow: As in the mean case, the shadowed object covariance calculation separates out the sky, or diffuse, irradiance contribution as

$$\Sigma_{LT} = f_T^2\{(1 - f_S)^2\Lambda_{LD1}g_{CT}\Sigma_{\rho T}\Lambda_{LD1}$$
$$+ f_{sky}^2[\Lambda_{LS1} - \Lambda_{LD1}]g_{CT}\Sigma_{\rho T}[\Lambda_{LS1} - \Lambda_{LD1}]\}$$
$$+ (1 - f_T)^2\Lambda_{LS1}g_{CB}\Sigma_{\rho Bm^*}\Lambda_{LS1}$$
$$+ [\Lambda_{LP1} - \Lambda_{LP0}]g_{CB}\Sigma_{\rho Bave}[\Lambda_{LP1} - \Lambda_{LP0}]. \tag{10}$$

B. Sensor Model

The sensor model takes the spectral radiance mean and covariance statistics for the various ground classes and applies sensor effects to produce signal mean and covariance statistics that describe the scene as imaged by an imaging spectrometer. The sensor model includes a limited number of radiometric noise sources, with no spatial or spectral sources of error included. Also, as was noted earlier, the channel spectral response of the sensor is applied during the input radiance calculations described in the previous section.

Radiometric noise processes are modeled by adding variance to the diagonal entries of the spectral covariance matrices. Off-diagonal entries are not modified, based on the assumption that there is no channel-to-channel correlation in the noise processes.

The radiometric noise sources come from detector noise processes, including photon (shot) noise, thermal noise, and multiplexer/readout noise. Since detector parameters are often specified in terms of electrons, the noise terms are summed in a root sum squared sense in that domain before being converted to noise equivalent spectral radiance. To calculate the photon noise term σ_{np}, the input radiance is converted to electrons and the square root taken as shown in (11). Note that this calculation is done for each object and background signal and for each spectral channel separately, with appropriate spectral variation for $L, \tau, \eta, \Delta\lambda, \lambda$

$$\sigma_{np} = \sqrt{L \times A\Omega \times \tau \times \eta \times t \times \Delta\lambda \times C_U \times \lambda/(h \times c)} \tag{11}$$

where

L input spectral radiance [mW/(cm^2-sr-μm)];
$A\Omega$ system throughput (cm^2-sr);
τ optical transmittance;
η quantum efficiency;
t integration time (in seconds);
$\Delta\lambda$ spectral channel bandwidth (μm);
λ spectral channel central wavelength (μm);
h Planck's constant $= 6.63 \times 10^{-34}$ J/s;
c the speed of light $= 3.0 \times 10^8$ m/s;
C_U unit conversion constant $= 10^{-9}$.

The total detector noise (in electrons) is then calculated as the root-sum-square of the photon noise σ_{np}, the thermal noise σ_{nt}, and the multiplexer/readout noise σ_{nm} as follows:

$$\sigma_n = \sqrt{\sigma_{np}^2 + \sigma_{nt}^2 + \sigma_{nm}^2}. \tag{12}$$

The total detector noise σ_n (in electrons) is then converted back to noise equivalent spectral radiance σ_{Ln} and scaled by a user-specified noise factor g_n before being added to the diagonal entries of the spectral covariance matrices as shown in (13) for each sensor spectral channel l

$$\Sigma_{Sm}^n(l, l) = \Sigma_{Sm}(l, l) + g_n^2\sigma_{Ln, l}^2. \tag{13}$$

The next noise source is relative calibration error c_R. This error is assumed to be uncorrelated between spectral channels, with a standard deviation σ_{CR} expressed as a percentage of the mean signal level. Thus, for each signal, this noise source is added as shown in (14)

$$\Sigma_{Sm}^{n+c}(l, l) = \Sigma_{Sm}^n(l, l) + [S_m(l) \times (c_R/100)]^2. \tag{14}$$

The last two noise sources are the quantization noise in the analog-to-digital conversion and bit errors in the communications or data recording system. These both depend upon the assumed dynamic range of the sensor $L_{\max}$. The quantization error variance is calculated as shown in (15)

$$\sigma_{nq}^2 = \frac{1}{12}\left(\frac{L_{\max}}{2^Q - 1}\right)^2. \tag{15}$$

The model for the effect of bit errors in the data link (or on-board storage) assumes that bit errors are uniformly distributed across the data word and could be of either sign. Thus,

for Q bits, the error will take on one of $2Q$ values, $\pm 2^i$ for $i = 0, \ldots, Q-1$, with equal probability of $1/(2Q)$. The noise variance, σ_{nBe}^2, due to a bit error rate of B_e is

$$\sigma_{nB_e}^2 = \frac{B_e}{Q} \sum_{q=0}^{Q-1} \left(2^q \frac{L_{\max}}{2^Q - 1} \right)^2. \tag{16}$$

These last two noise terms σ_{nq}^2 and σ_{nBe}^2 are added to the diagonal entries of the spectral covariance matrices in a manner similar to the calibration error in (14).

The class-dependent sensor signal-to-noise ratio (SNR) is calculated as the ratio between the mean signal and the square root of the sum of the noise variance terms as shown in (17), where m is either the object or one of the background classes

$$\text{SNR}_m = \frac{S_m}{\sqrt{\sigma_{Lnm}^2 + \sigma_{CR}^2 + \sigma_{nq}^2 + \sigma_{nBe}^2}}. \tag{17}$$

C. Processing Model

1) Atmospheric Compensation: Atmospheric compensation is accomplished by defining surrogate low and high reflectance calibration panels and computing the slope m and offset o of a two-point linear fit between the mean panel signals and the known reflectances. This models the empirical line method (ELM) often used for atmospheric compensation.

The slopes and offsets are applied to the mean signal and covariance matrices of the object and background classes to compute the retrieved (or estimated) class reflectance mean $\hat{\rho}$ and covariance $\hat{\Sigma}$ statistics.

2) Feature Selection: Several options are available for extracting a reduced dimensionality feature vector from the signal vector:

1) all channels within contiguous region(s), (e.g., to avoid water vapor absorption spectral regions);
2) principle components;
3) band averaging to simulate multispectral channels.

Each option is implemented as a linear transformation using an appropriate feature selection matrix Ψ. This matrix is applied to both the mean vectors and the covariance matrices in either the retrieved reflectance domain (if atmospheric compensation was performed) or in the signal domain directly on the statistics output by the sensor model, as shown in (18) and (19)

$$F_m = \Psi^T X_m \tag{18}$$
$$\Sigma_{Fm} = \Psi^T \Sigma_{Xm} \Psi. \tag{19}$$

In (18) and (19), the variable X refers to the signal type (retrieved reflectance or sensor signal) and the index m refers to the various object and background classes.

3) Performance Metrics: Three algorithms are available to determine a performance metric for a given scenario: 1) spectral characterization accuracy, 2) a version of a spectral matched filter known as constrained energy minimization (CEM) [17], and 3) total error. The spectral characterization accuracy is a measure of how well the spectral reflectance can be retrieved from the sensor measurements. The matched filter can be used to predict probability of detection versus probability of false alarm

(P_D/P_{FA}) curves. Total error approximates the sum of false alarm and missed detection probabilities to produce a scalar performance metric.

The first performance metric, spectral characterization accuracy, is quantified by the mean difference, SC_{bias}, between the retrieved surface reflectance of the object and its initial known reflectance, and by the standard deviation, σ_{SC}, of the difference for each spectral channel l, as in

$$SC_{bias}(l) = \hat{\rho}(l) - \rho(l) \tag{20}$$

$$\sigma_{SC}(l) = \sqrt{\hat{\sigma}_\rho^2(l, l) - \sigma_\rho^2(l, l)}. \tag{21}$$

The second performance metric, the matched filter, uses a known object "signature" and an estimate of the background spectral covariance to minimize the energy from the background and to emphasize the desired object. The filter operator w is formed as shown in (22), where the subscript F indicates the signal means and covariances have been transformed to the desired feature space using (18) and (19). In the model implementation, the known "signature" ρ_T is the original object mean spectral reflectance used at the input to the model. The estimates of the average background mean $\hat{\rho}_{Bave}$ and covariance $\hat{\Sigma}_{Bave}$ are the ones obtained after the effects of the imaging system and atmospheric compensation have been applied

$$w = \frac{\hat{\Sigma}_{\rho FBave}^{-1}(\rho_{FT} - \hat{\rho}_{FBave})}{(\rho_{FT} - \hat{\rho}_{FBave})^T \hat{\Sigma}_{\rho FBave}^{-1}(\rho_{FT} - \hat{\rho}_{FBave})}. \tag{22}$$

This operator w is then used to transform the means and covariances from the feature space to a scalar test statistic with mean θ and variance σ_θ^2, from which the P_D/P_{FA} curve can be calculated. The operator is applied to the combined object/background features and to the features of each background class as

$$\theta_T = w^T(\hat{\rho}_{FT} - \hat{\rho}_{FBave}) \tag{23}$$
$$\theta_{Bm} = w^T(\hat{\rho}_{FBm} - \hat{\rho}_{FBave}) \qquad \text{for } m = 1 \cdots M \tag{24}$$
$$\sigma_{\theta_T}^2 = w^T \hat{\Sigma}_{\rho FT} w \tag{25}$$
$$\sigma_{\theta_{Bm}}^2 = w^T \hat{\Sigma}_{\rho FBm} w \qquad \text{for } m = 1 \cdots M. \tag{26}$$

The probability of detection P_{Dm} (computed separately for each background class m) is then computed for a user-specified probability of false alarm P_{FA}, using a Gaussian assumption for the test statistic output probability density function. This assumption is somewhat justified by the Central Limit Theorem since the operator is a summation of a large number of random variables. The section on validation discusses this assumption further. The threshold h_m is determined from the desired probability of false alarm and from the mean θ_{Bm} and variance $\sigma_{\theta_{Bm}}^2$ of each background class m as shown in (27). The function Φ^{-1} returns the cutoff value such that the area under the standard normal curve to the right of the cutoff is equal to the argument of the function. The probability of detecting the object in background class m is shown in (28)

$$h_m = \theta_{Bm} + \sigma_{\theta_{Bm}} \Phi^{-1}(P_{FA}) \tag{27}$$

$$P_{Dm} = \frac{1}{\sigma_{\theta_T} \sqrt{2\pi}} \int_{h_m}^{\infty} \exp\left[-\frac{(x - \theta_T)^2}{2\sigma_{\theta_T}^2} \right] dx. \tag{28}$$

For scenarios with multiple backgrounds, the threshold h^* yielding the minimum P_D is used to recompute the P_{FA}'s for the other classes. These new P_{FA}'s are then summed using the background class area fractions f_m to yield a combined P_{FA} as shown in (29). The combined P_D is simply the minimum P_{Dm} as shown in (30)

$$P_{FA} = \sum_{m=1}^{M} f_m P_{FAm}(h^*) \tag{29}$$

$$P_D = \min P_{Dm}. \tag{30}$$

The third performance metric included in the model is the total error metric. It approximates the total error P_e (i.e., the overlap between multivariate distributions) in a two-class equal *a priori* probability case [18] as

$$P_e \approx \tfrac{1}{2}(1 - P_D) + \tfrac{1}{2} P_{FA}. \tag{31}$$

While P_e does not distinguish between errors due to false alarms or missed detections, it does provide a single scalar metric that can be used for relative performance comparisons. It is normally used in the model to assess the relative contribution to system error from the various system parameters, as shown in the section on example results. P_e is calculated using the standard normal error function and the Bhattacharyya distance B

$$P_e = \frac{1}{\sqrt{2\pi}} \int_{\sqrt{2B}}^{+\infty} \exp\left(-\frac{x^2}{2}\right) dx \tag{32}$$

where

$$B = \frac{1}{8}(F_T - F_B)^T \left(\frac{\Sigma_{FT} + \Sigma_{FB}}{2}\right)^{-1} (F_T - F_B)$$

$$+ \frac{1}{2} \ln \frac{\left|\frac{\Sigma_{FT} + \Sigma_{FB}}{2}\right|}{\sqrt{|\Sigma_{FT}||\Sigma_{FB}|}}. \tag{33}$$

D. Model Implementation

The model has been implemented as part of a software package developed at Lincoln Laboratory named Forecasting and Analysis of Spectroradiometric System Performance (FASSP). The package is written in the Interactive Data Language (IDL) of Research Systems Incorporated, taking advantage of the integrated Graphical User Interface (GUI) and plotting capabilities, as well as the portability between computing platforms.

The scene, sensor, and processing parameters are specified by the user through a scenario parameter file loaded into FASSP. These values may be modified through the GUI. A software control executive allows trade studies to be conducted automatically for a number of parameters. A typical parameter trade study takes only a few minutes on a UNIX workstation.

III. VALIDATION

The validation of the model and its implementation has been studied with airborne hyperspectral imagery. Observed empirical data and the model predictions have been compared at several points in the end-to-end spectral imaging process. These validation points include the spectral radiance at the sensor input aperture, the sensor signal-to-noise ratio, and the detection performance (P_D/P_{FA}) after application of a spectral matched filter. While the experiments described below do not constitute a comprehensive validation of the model, they do confirm the representative nature of the model as well as provide insights into the model's accuracy and limitations.

The data used in this process were collected by the airborne HYDICE sensor [3] as part of field experiments during which substantial ground truth was collected.
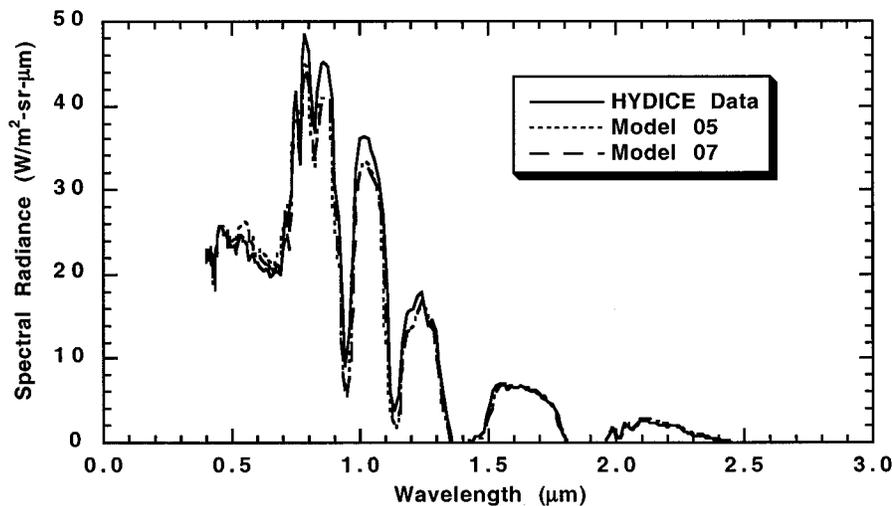
A. Spectral Radiance Statistics

This case compared the measured and predicted radiance statistics of a man-made object deployed on an open grassy field. The HYDICE data-derived mean and standard deviation, shown in Fig. 2, were calculated from Run 07 of a data collection on August 24, 1995. To model this case, input parameters, such as the solar zenith angle and other atmospheric conditions, were chosen to be as similar as possible to the actual scene conditions. The model was run using two different sources of the input reflectance statistics. The first case (labeled "Model 05") used data from a HYDICE image of the scene collected earlier that day from a lower altitude and converted to reflectance using the Empirical Line Method (ELM). This provided an "independent" data source. The second case (labeled "Model 07") used reflectance statistics derived from the same HYDICE image as was used to calculate the mean and standard deviation of the sensor-measured spectral radiance (curves labeled "HYDICE Data" in Fig. 2).

Reflectance statistics derived from the HYDICE data (rather than field spectrometer measurements) were used as model inputs in this comparison for several reasons. First, since we wanted to confirm the model transformation of surface reflectance variability to radiance variability, it was desirable to have a large number of samples to obtain good statistics. The ground truth had typically only a few samples per object, while the imagery provided tens to thousands of samples (pixels). Another factor affecting the appropriateness of the variability is the significantly smaller spatial field of view of the field spectrometer in this case compared to the pixel size of the imagery. As was observed, and is discussed below, the spatial resolution affects the measured variability for nonuniform surfaces like the man-made object studied here. Lastly, we observed significant errors in the ground truth measurements, leading to a conclusion that the airborne data was more appropriate in this case.

The two predicted mean spectral radiance curves shown in Fig. 2(a) are generally within 5%–10% of the measured values. This level of discrepancy is within the absolute calibration error of the sensor and possible errors due to differences between the real atmosphere and the assumed MODTRAN model atmosphere. Since our goal is to confirm the model implementation, and not to study the sensor calibration nor validate MODTRAN, these differences were judged to be reasonable.

The spectral radiance standard deviations shown in Fig. 2(b) show significant differences between the "Model 05" prediction and the measured data, but a much closer match for the

a) Mean spectral radiance
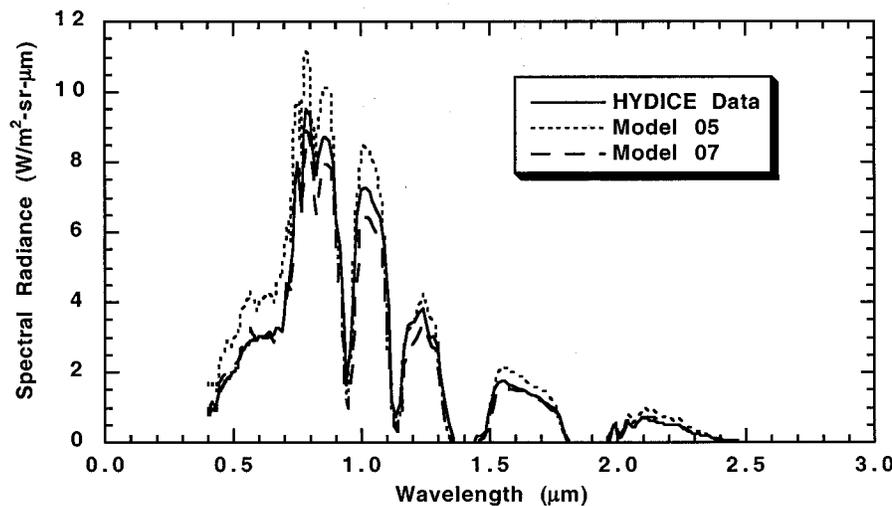
b) Spectral radiance standard deviation

Fig. 2. Comparison of calibrated airborne hyperspectral spectral radiance from the HYDICE sensor with model predicted spectral radiance using similar conditions. The two model curves in each plot differ in the source of the spectral reflectance data used in the model. The curves labeled "Model 05" used HYDICE data from an earlier flight while those labeled "Model 07" used data from the same flight as was used for the "HYDICE Data" curves.

"Model 07" prediction. These results may be partly explained by the different spatial resolutions of the data used to derive the reflectance statistics input to the model. The data used by the model for the "Model 05" case were at a resolution of $\sim$0.75 m, while the "Model 07" (and the measured HYDICE data shown in the plots) had a resolution of $\sim$1.5 m. It has been observed that higher spatial resolution often leads to greater variance in the spectral domain [19]. The results of Fig. 2(b) are consistent with this observation. The differences between the "Model 05" and "HYDICE Data" curves show a typical magnitude of discrepancy in modeling spectral radiance variations that can come from inconsistencies in the resolutions of data. The good match between the "Model 07" and "HYDICE Data" show the model is propagating the reflectance variance into spectral radiance variance, as shown in (7), in a consistent manner.

B. Sensor SNR

A detailed list of parameters measured by the HYDICE manufacturer [20] was used to implement a radiometric sensor model that captured the dominant noise mechanisms. For this experiment, the model's prediction was compared to an empirical measurement of the HYDICE SNR calculated for its design scene of a 5% albedo surface, a 60° solar zenith angle, and the 1976 US standard atmosphere, as shown in Fig. 3. The empirical result for HYDICE was calculated using simulated radiance as the signal, and with noise computed as the standard deviation of HYDICE calibration frames with the on-board calibration lamp providing the illumination. The comparison was done for two integration times as shown, and the predictions compare closely to the measured results. Since the SNR is seen to be proportional to the pixel integration time
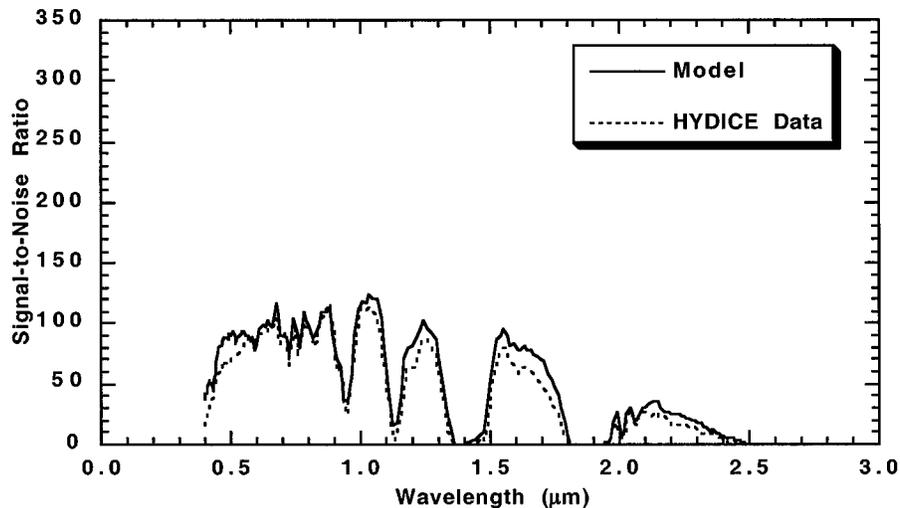
a) Pixel integration time = 5 msec
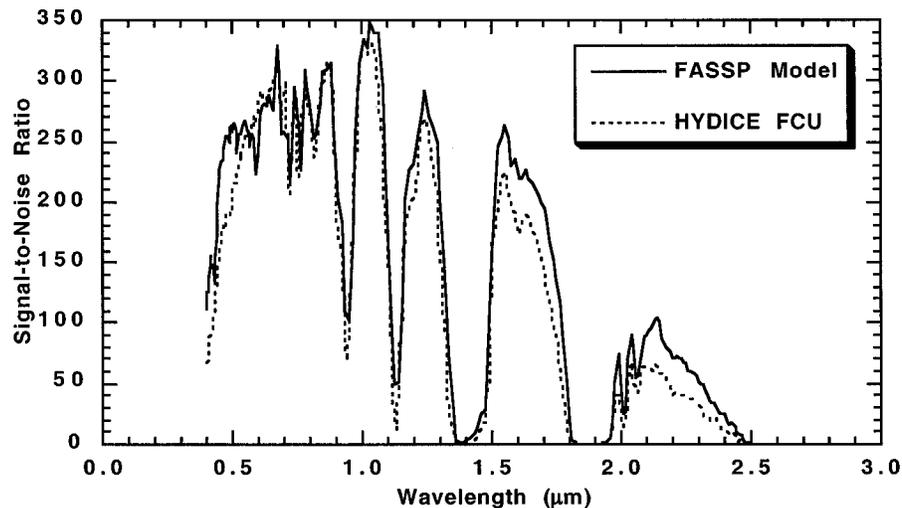
b) Pixel integration time = 15 msec

Fig. 3.   Comparison of SNR calculated from HYDICE sensor data to model prediction for similar conditions.

at these relatively low signal levels, one can conclude that the instrument is fixed noise limited. Thus, at these signal levels, the instrument noise level is not signal-dependent, and the use of the simulated radiance for the signal is seen to be a valid approach.

C. Receiver Operating Characteristic Curve

A critical aspect of the validation of an end-to-end model is at the output, which, for the scenario of subpixel object detection, is the detection probability at a specified probability of false alarm. This is a point on the receiver operating characteristic (ROC) curve. The ROC curve characterizes the tradeoff in these probabilities as a function of a varying detection threshold. Since a parameter of interest in subpixel detection applications is the smallest fraction of a pixel an object can occupy and still

be detectable, we often use a modified version of the ROC curve which shows the detection probability at a constant false alarm rate (CFAR) as a function of object pixel fill fraction.

For this experiment, two HYDICE images collected on August 24, 1995 were concatenated to provide an adequate homogenous background sample size. The images contained open grass fields, forests, and gravel roads, along with a number of resolved objects. The background pixels were first classified into relatively homogeneous regions and 110 040 open grass pixels identified as belonging to a unimodal distribution. 339 pixels from several man-made objects with similar surfaces were also identified and used to simulate subpixel objects in the open grass background pixels at varying fractions using the linear mixing model.

An analogous model scenario was set up using background and object statistics derived from HYDICE imagery collected

over the same site, but from an independent run, and converted to spectral reflectance using ELM. The model atmospheric and illumination conditions were specified to be similar to those at the time of the data collect.

A spectral matched filter was developed and applied in each of the empirical and model scenarios using the mean of the object spectra as the object signature, and the background covariance matrix. For the empirical case, a threshold was first determined such that the number of background pixels with a filter output exceeding that threshold corresponded to the desired false alarm rate. The, P_D was calculated, for each fill fraction, based on the number of subpixel object pixels whose filter output exceeded that threshold. The model P_D's were calculated using the Gaussian assumption as described in equations (27) and (28). Fig. 4 shows the comparison between predicted and observed detection probability as a function of object pixel fill fraction, for two false alarm rates. As can be seen, there are some differences in the P_D between the empirical and model results, but overall the model shows a similar trend. An interpretation of this result is that both the model prediction and the empirical data analysis suggest that this object is detectable ($P_D \geq 0.8$, $P_{FA} \leq 10^{-5}$) at pixel fractions greater than 25% in this background. Differences between the model prediction and the empirical result can be explained by a variety of factors including

1) background and object pixels in empirical data were not identical to pixels used to derive statistics for model input;
2) possible residual artifacts in the HYDICE data that were not modeled;
3) the matched filter output test statistic was not Gaussian, as the model assumes.

This last point is an important consideration because the model relies on being able to transform the first- and second-order statistics of the classes into parameters that can be used in an analytical expression to predict performance. Although we have observed data sets where this Gaussian assumption holds for appropriately screened backgrounds, the true form of the matched filter output statistical distribution for natural backgrounds and man-made objects is an active area of investigation [7], [21]. As results of those investigations become available, we will seek to incorporate the findings into the model. In the meantime, we will continue to use the Gaussian assumption for the matched filter output as it has been shown to provide valuable results.

IV. EXAMPLE RESULTS

A. Relative Roles of System Parameters

One advantage of an end-to-end system model is the user controls all the scene, sensor, and processing parameters and can specify nearly arbitrary configurations. Our model includes an option to automatically study the relative role of system parameters in a quantitative manner. As an example, we consider the problem of detecting subpixel roads in a grass background. This application could arise in the use of moderate spatial resolution hyperspectral imagery to derive a road network layer for a Geographic Information System (GIS). In this example, we used the modeled HYDICE sensor flying at 6 km and reflectance statis-
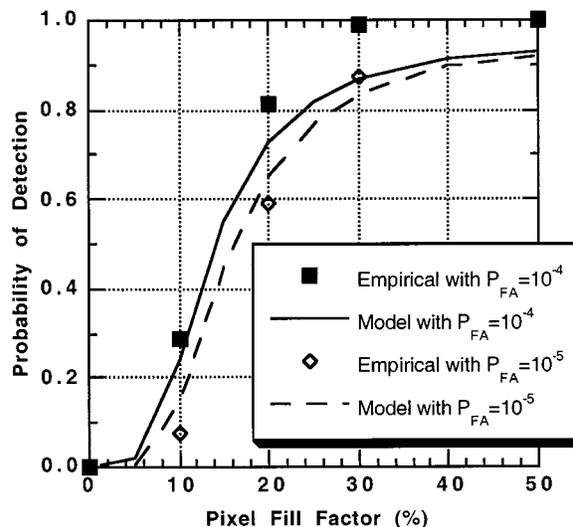

Fig. 4. Comparison of empirical detection performance using airborne hyperspectral imagery to predictions made with model for similar conditions.

tics for a gravel road and a grass field derived from measured HYDICE data.

The analysis is conducted by calculating the total error P_e with all parameters at their nominal values, and then recalculating the P_e as each of the parameters is changed to an excursion value, while leaving all other parameters at their nominal value. Each parameter excursion value is chosen to represent either an ideal value or one that would have a minimal effect on system performance. Table III lists the system parameters studied, their nominal values, their excursion values, the model-calculated probability of error, and a quantitative estimate of the relative importance to system performance of each parameter. The P_e metric is used as a representation of the separability of the subpixel road class and the grass background. The relative role of each parameter is then calculated by taking the difference between the error calculated using the excursion value of that parameter and the system nominal error, and then normalizing by the sum of all such differences.

The results shown in Table III indicate that the most important system parameters are subpixel fraction, the grass background covariance, and the meteorological range (atmospheric visibility), and each has about the same relative role. The number of spectral channels has the next biggest influence, then the sensor view angle, and so on. Of interest is that the impact of off-nadir viewing is predicted to be more significant than an off-zenith solar angle. Although the model does not take into account the BRDF of the surface, this result can be explained by the increase in the path radiance scattered into the sensor aperture, which, because of the "adjacency effect" [16], has the impact of reducing separability between the road and the grass classes.

It is important to note that the conclusions of this type of analysis are extremely dependent upon the scenario configuration and the system parameters considered. The results shown in Table III are not intended to apply to the general case, but are shown to illustrate a use of the model and a methodology for quantitatively assessing the relative importance of diverse system parameters in an end-to-end spectral imaging system.

TABLE III
RELATIVE ROLE OF SYSTEM PARAMETERS SUB-PIXEL ROAD DETECTION SCENARIO: $P_e = 0.0427$ WITH ALL NOMINAL VALUES

Scenario Parameter	Nominal Value	Excursion Value	P_e for Excursion Value	Relative Role
Object pixel fraction	0.25	1.00	.0000	18%
Background variability scaling factor	1	0	.0000	18%
Meteorological range	8 km	50 km	.0007	18%
Number of spectral channels	30	60	.0051	16%
Sensor nadir view angle	45°	0°	.0115	13%
Sensor relative calibration error	1%	0%	.0218	9%
Object variability scaling factor	1	0	.0323	5%
Solar zenith angle	45°	0°	.0368	3%
Sensor noise scaling factor	1	0	.0421	0%
Number of radiometric bits	12	16	.0426	0%
Bit error rate	10^{-9}	0	.0427	0%
Total				100%

TABLE IV
ROAD DETECTION SCENARIO

Scenario Parameter	Nominal Value
Object pixel fraction	Variable
Meteorological range	16 km
Solar zenith angle	45°
Sensor nadir view angle	0°
Sensor relative calibration error	1%
Sensor noise scaling factor	1
Number of radiometric bits	12
Bit error rate	10^{-9}
Number of spectral channels	121
Spectral processing algorithm	CEM Spectral Matched Filter
False Alarm Rate (per pixel)	10^{-5}

B. Subpixel Detection Sensitivity to Various System Parameters

Another use of the model is to study how sensitive a given sensor might be to either design changes or scene conditions. This type of analysis can be helpful when setting system requirements or when setting data collection parameters for systems which have controllable parameters.

To illustrate this use of the model, we present three examples showing parameter sensitivities. The scenario for all three is the detection of subpixel roads in a hyperspectral image, similar to the previous example, but with the use of a road spectrum (from a library or previous data collection) and a spectral matched filter. The analyses assume a HYDICE-like sensor, with similar spectral and radiometric properties, and an atmospheric compensation algorithm with 1% accuracy. Table IV presents other parameters and values assumed in the analyses.

In the first two examples given below, the road is assumed to be subpixel in a grass background, while the third example considers the impact of multiple background classes. In all cases, the results are presented as the probability of detection (at a constant false alarm rate) as a function of the fraction of a pixel occupied by road material. This pixel fill fraction can be loosely translated to an actual object size, given a pixel ground resolution, assuming the object is not split across adjacent pixels. As an example, a 5-m-wide road running through the middle of a 10-m resolution pixel would roughly correspond to a 50% fill factor, ignoring the detailed effects of sensor

and atmospheric point spread functions. Because the model assumes a linear mixing of the object and the background class, we can present P_D as a function of this pixel fill fraction and avoid specifying a particular sensor spatial resolution and object size. Thus, the analysis results can be applied to a range of absolute ground resolutions and object sizes, although the exact performance will vary because of sensor noise considerations and the variability of the spectral statistics at the various resolutions.

1) Sensitivity to Atmospheric Meteorological Range: Changes in atmospheric visibility, specified by the meteorological range parameter, will affect the signal level in a spectrally-dependent manner, as well as affect the amount of radiance scattered from the background into the object pixel. Even though the scenario includes an atmospheric compensation step, this scattered radiance can affect performance. Fig. 5 shows that the required fill fraction f_T for a high detection probability ($P_D \geq 0.9$) increases with decreasing meteorological range. However, the increase in required f_T is relatively small (10% to 12%) for a significant decrease (64 km to 4 km) in the meteorological range. Thus, in this scenario, one can conclude that detection performance is not significantly affected by atmospheric haze over a reasonable range of values.

2) Sensitivity to Random Calibration or Compensation Errors: The effects of random error in this analysis are studied by adding zero-mean "noise" with a standard deviation σ equal
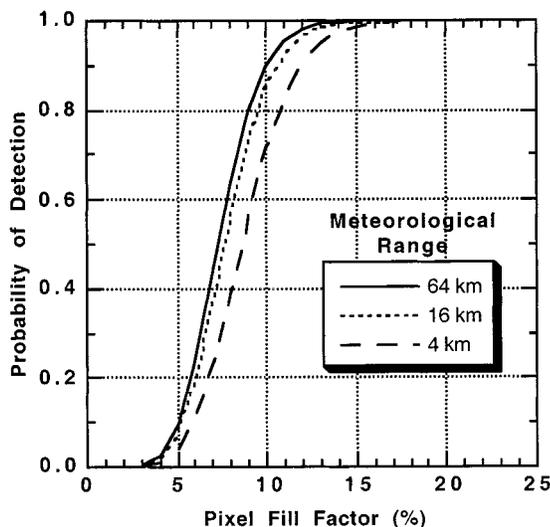
Fig. 5. Sensitivity of road detection performance to atmospheric meteorological range as a function of pixel fill fraction.
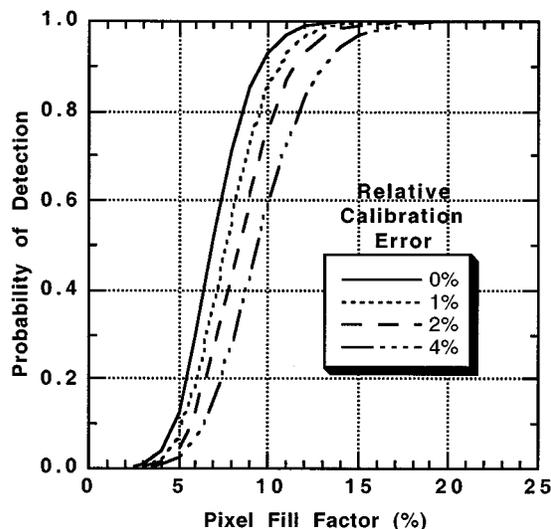

Fig. 6. Sensitivity of road detection performance to additional (beyond sensor detector and electronics noise) random error (with a standard deviation expressed as a percentage of the mean signal) as a function of pixel fill fraction.

to a user-specified percentage of the mean radiance. In a real sensor system, this random error could come from a number of sources such as residual nonuniformity correction error or random errors in the atmospheric compensation.[2] Fig. 6 presents the sensitivity of detection probability to random errors of 0%, 1%, 2%, or 4% of the mean signal level. This range of additive error is typical for state-of-the-art sensors, nonuniformity correction routines, and atmospheric compensation algorithms. As in the previous example, for this range of values, the detection performance sensitivity is not too significant, with the fill fraction required for $P_D \geq 0.9$ changing from 9% to 13%, as 4% additional error is added.

3) Sensitivity to Multiple Scene Classes: The previous examples assumed a situation where the scene contained subpixel roads in a homogeneous grass background. Most real images of interest will contain multiple background classes in the scene. The additional classes affect the analysis results in two ways. First, the background covariance used in the matched filter [Eq. (22)] is assumed to be calculated using data from the entire scene. Thus, the detection operator w is different for different combinations of backgrounds. Second, the detection operator is applied to each of the class statistics individually, and the detection probability is determined by the class with the lowest P_D [see (29) and (30)].

Table V lists the background classes and their area percentages for three cases. The "Grass only" case repeats the situation from the previous example using a 16 km meteorological range and 1% random error. The "Mixture 1" and "Mixture 2" cases show the results when the scene has multiple background classes (also with 16 km meteorological range and 1% random error).

As can be seen in Fig. 7, the addition of several vegetation classes ("Mixture 1") did not significantly change the fill fraction at which high P_D can be achieved. However, the addition of the two "roof" categories in "Mixture 2" significantly raised the fill fraction required for high P_D. In particular, the "light roof"

class has a spectrum very similar to the road spectrum, with the consequence of high false alarm rates at low road subpixel fractions.

This result is intuitive and has been observed in the analysis of real hyperspectral imagery. Often, analysts will improve their processed results by applying a sequence of algorithms to mitigate false alarms from confusing materials. Our model does not directly take this into account, and thus we often will conduct analyses with single backgrounds. This represents a situation where an analyst might perform a classification (or clustering) of the image pixels first, and then construct separate matched filters, using the same object spectrum, but different background covariances estimated only from samples in the various classes [22]. Thus, the problem is reduced to finding the material in a single, relatively homogenous, background class.

V. SUMMARY AND CONCLUSIONS

An approach has been presented to predict detection performance, analyze sensitivities, and determine relative contributions of system parameters for multispectral or hyperspectral sensors used in the detection of subpixel objects. The end-to-end system model builds on a previously developed approach using first- and second-order spectral statistics and transformations of those statistics to predict performance. Enhancements include a linear mixing model for the subpixel objects, additional sensor modeling capability, atmospheric compensation approaches, and a matched filter detection algorithm. Unlike image simulation models, this model does not produce a simulated image, but rather predicts detection or error probabilities. Thus, our model avoids the computational requirements for pixel-by-pixel ray tracing of simulation approaches.

The model has been, and continues to be, validated by showing good agreement between predictions and measurements of spectral radiances, sensor SNRs, and detection probabilities derived from airborne hyperspectral sensor data.

---

[2]Another way to interpret these error levels is to recognize that with the additive error, the spectral radiance in each spectral channel has a signal-to-noise ratio hard limited to the inverse of the additive error. For example, with 2% random error added, the SNR cannot be higher than 50.

TABLE V
BACKGROUNDS FOR ROAD DETECTION SCENARIO

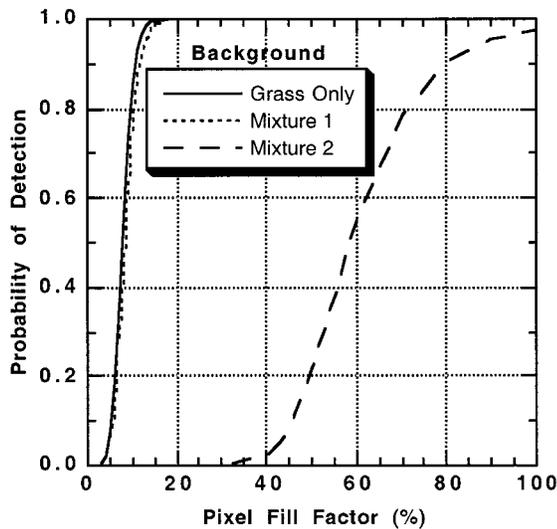| Background Label	Classes and % of Scene
Grass Only	100% Grass
Mixture 1	50% Grass, 30% Trees, 15% Shaded Trees, 5% Bushes
Mixture 2	40% Grass, 30% Trees, 15% Shaded Trees, 5% Bushes, 5% Light Roofs, 5% Dark Roofs

Fig. 7. Sensitivity of road detection performance to additional classes (defined in Table V) in the scene as a function of pixel fill fraction.

assess the appropriate statistical distributions for various classes of hyperspectral data, as well as develop confidence intervals for detection probability predictions using appropriate models for the variability of the contributing factors.

An example analysis was presented that showed which system parameters were most important in a given scenario. Also, examples were presented predicting detection performance sensitivity to atmospheric, sensor, and scene parameters. In the cases examined, the most important and most sensitive parameters were characteristics of the surface classes and environmental conditions of the scene, rather than sensor parameters or algorithmic choices. Certainly, though, situations exist where these parameters or choices can have significant effect.

The model has many advantages over other performance prediction tools, including quick execution, which enables extensive trade studies to be conducted expeditiously. It does, however, have a number of limitations, some of which can be addressed with further development, while others are inherent in the analytical approach. Limitations that are inherent include the inability to model specific geometries of scene objects or materials, especially those that involve multiple reflections, and sensor artifacts or processing algorithms that involve nonlinear operations.

Limitations of the model that we plan to address through additional development include implementation of additional sensor types and artifacts (e.g., Fourier transform instruments, spectral jitter, and calibration error) and processing algorithms (e.g., physics-based atmospheric compensation, anomaly detection, linear unmixing, material identification). Also, we continue to

REFERENCES

[1] H. J. Kramer, Observation of the Earth and Its Environment: Survey of Missions and Sensors, 2nd ed. New York: Springer-Verlag, 1994.
[2] R. O. Green, M. L. Eastwood, C. M. Sarture, T. G. Chrien, M. Aronsson, B. J. Chippendale, J. A. Faust, B. E. Pavri, C. J. Chovit, M. Solis, M. R. Olah, and O. Williams, "Imaging spectroscopy and the airborne visible/infrared imaging spectrometer (AVIRIS)," Remote Sens. Environ., vol. 65, pp. 227–248, 1998.
[3] L. J. Rickard et al., "HYDICE: An airborne system for hyperspectral imaging," Proc. SPIE Imag. Spectro. Terrest. Environ., vol. SPIE-1937, 1993.
[4] J. Pearlman, C. Segal, L. Liao, S. Carman, M. Folkman, S. Ungar, W. Browne, and L. Ong, "Development and operations of the EO-1 Hyperion imaging spectrometer," Proc. SPIE Earth Observ. Syst. V, vol. SPIE-4135, pp. 243–253, 2000.
[5] M. E. Martin, S. D. Newman, J. D. Aber, and R. G. Congalton, "Determining forest species composition using high spectral resolution remote sensing data," Remote Sens. Environ., vol. 65, pp. 249–254, 1998.
[6] G. Healey and D. Slater, "Models and methods for automated material identification in hyperspectral imagery acquired under unknown illumination and atmospheric conditions," IEEE Trans. Geosci. Remote Sensing, vol. 37, pp. 2706–2717, Nov. 1999.
[7] D. Manolakis, C. Siracusa, and G. Shaw, "Hyperspectral subpixel target detection using the linear mixing model," IEEE Trans. Geosci. Remote Sensing, vol. 39, pp. 1392–1409, July 2001.
[8] "Special issue on analysis of hyperspectral image data," IEEE Trans. Geosci. Remote Sensing, vol. 39, pp. 1343–1539, July 2001.
[9] J. P. Kerekes and D. A. Landgrebe, "An analytical model of Earth-observing remote sensing systems," IEEE Trans. Syst., Man, Cybern., vol. 21, pp. 125–133, Jan./Feb. 1991.
[10] ——, "Parameter trade-offs for imaging spectrometer systems," IEEE Trans. Geosci. Remote Sensing, vol. 29, pp. 57–65, Jan. 1991.
[11] C. R. Schwartz, A. C. Kenton, W. F. Pont, and B. J. Thelen, "Statistical parametric signature/sensor/detection model for multispectral mine target detection," Proc. SPIE, vol. 2496, 1995.

[12] B. V. Shetler, D. Mergens, C. Chang, F. C. Mertz, J. R. Schott, S. Kubica, R. K. deJonckheere, and B. C. Tousley, "Comprehensive hyperspectral system simulation: I. Integrated sensor scene modeling and the simulation architecture," *Proc. SPIE Alg. Multispect., Hyperspect., Ultraspect. Imag.*, vol. SPIE-4049, 2000.

[13] R. J. Bartell, C. R. Schwartz, M. T. Eismann, J. N. Cederquist, J. A. Nunez, L. C. Sanders, A. H. Ratcliff, B. W. Lyons, and S. D. Ingle, "Comprehensive hyperspectral system simulation: II. Hyperspectral sensor simulation and preliminary VNIR testing results," *Proc. SPIE Alg. Multispect., Hyperspect., Ultraspect. Imag.*, vol. SPIE-4049, 2000.

[14] J. R. Schott, *Remote Sensing: The Image Chain Approach*. New York: Oxford Univ. Press, 1997.

[15] A. Berk, L. S. Bernstein, and D. C. Robertson, "MODTRAN: A moderate resolution model for LOWTRAN 7," Spectral Sciences, Burlington, MA, GL-TR-89-0122, 1989.

[16] Y. J. Kaufman, "Atmospheric effect on spatial resolution of surface imagery," *Appl. Opt.*, vol. 23, no. 19, pp. 3400–3408, Oct. 1984.

[17] W. H. Farrand and J. C. Harsanyi, "Mapping the distribution of mine tailings in the Coeur d'Alene River Valley, ID, through the use of a constrained energy minimization technique," *Rem. Sens. Environ.*, vol. 59, pp. 64–76, 1997.

[18] S. J. Whitsitt and D. A. Landgrebe, "Error estimation and separability measures in feature selection for multiclass pattern recognition," Lab. Applicat. Remote Sensing, Purdue Univ., West Lafayette, IN, LARS Pub. 082 377, Aug. 1977.

[19] B. G. Mobasseri, P. E. Anuta, and C. D. McGillem, "A parametric model for multispectral scanners," *IEEE Trans. Geosci. Remote Sensing*, vol. GE-18, pp. 175–179, Apr. 1980.

[20] R. Basedow, Raytheon Opt. Syst., Inc., Danbury, CT, private communication, 1999.

[21] D. G. Manolakis, J. P. Kerekes, and G. A. Shaw, "Statistics of hyperspectral imaging data," *Proc. SPIE Alg. Multispect., Hyperspect., Ultraspect. Imag.*, vol. SPIE-4381, 2001.

[22] C. C. Funk, J. Theiler, D. A. Roberts, and C. C. Borel, "Clustering to improve matched filter detection of weak gas plumes in hyperspectral thermal imagery," *IEEE Trans. Geosci. Remote Sensing*, vol. 39, pp. 1410–1420, July 2001.

John P. Kerekes (S'81–M'89–SM'00) received the B.S., M.S., and Ph.D. degrees in electrical engineering from Purdue University, West Lafayette, IN, in 1983, 1986, 1989, respectively.

From 1983 to 1984, he was Member of Technical Staff with the Space and Communications Group of the Hughes Aircraft Co., El Segundo, CA, where he performed circuit design for communications satellites. From 1986 to 1989, he was a Graduate Research Assistant, working with both the School of Electrical Engineering and the Laboratory for Applications of Remote Sensing at Purdue University. Since 1989, he has been with the Massachusetts Institute of Technology Lincoln Laboratory, Lexington, modeling sensor system performance in pattern recognition and geophysical parameter retrieval applications.

Dr. Kerekes is a member of Tau Beta Pi, Eta Kappa Nu, American Geophysical Society, American Meteorological Society, and the American Society for Photogrammetry and Remote Sensing. Since 1995, he has served as the Chair of the Boston Section Chapter of the IEEE Geoscience and Remote Sensing Society.

Jerrold E. Baum received the A.B. degree from Brandeis University, Waltham, MA, in 1975 and the M.S. degree from University of Maryland, College Park, in 1980, both in physics.

From 1977 to 1985, he taught high school physics in Maryland and Massachusetts. In 1985, he joined Textron Defense Systems, Wilmington, MA, as a Senior Engineer, where he helped develop the detection algorithm for an airborne infrared sensor. Since 1989, he has been an Associate Staff Member at the Massachusetts Institute of Technology Lincoln Laboratory, Lexington. He is currently involved with modeling and analyzing hyperspectral remote-sensing systems. His previous work included analyzing GOES imager satellite data, modeling infrared sensor performance in battlefield simulations, and evaluating active- and passive-infrared detection algorithms.